PERGAMON

International Journal of Heat and Mass Transfer 42 (1999) 2269–2285

International Journal of HEAT and MASS TRANSFER

Convective film cooling over a representative turbine blade leading-edge

Siddharth Thakur, Jeffrey Wright, Wei Shyy*

Department of Aerospace Engineering, Mechanics and Engineering Science, University of Florida, Gainesville, FL 32611, U.S.A.

Received 28 August 1997; in final form 18 March 1998

Abstract

Computations are performed to simulate a discrete hole film cooling flow over an experimental test geometry representative of the leading edge of turbine blades. A multiblock pressure correction algorithm is used for the computations, and both low-Reynolds number and wall function k–ε models are used for turbulence closure. The flow through the coolant ducts, from the plenum to the blade surface, is resolved as a part of the computation by specifying the coolant mass flux in the plenum. A systematic grid refinement study is conducted with the finest grid consisting of approximately one million points. Next, the flowfield is examined; key physical mechanisms resulting from the interactions between the cooling jets and the freestream are identified and their effect on the thermal field is compared with the experimentally observed thermal field. Finally, a study of geometric parametric variation is conducted to optimize the film cooling design. Nine different combinations of two parameters, namely, the relative stagger and the relative angle between the two rows of cooling holes are investigated for their effect on heat transfer on the blade surface.

Nomenclature

D hole diameter
k turbulent kinetic energy
P production of turbulent kinetic energy
s streamwise coordinate along the blade surface measured from the symmetry plane
u, v, w Cartesian velocity components
U freestream or coolant velocity
x, y, z Cartesian coordinates
y^+ non-dimensionalized distance from wall (wall coordinates)
z spanwise coordinate on the blade surface.

Greek symbols

ε rate of dissipation of turbulent kinetic energy
μ molecular viscosity
μ_t turbulent (eddy) viscosity
η surface adiabatic effectiveness
ϱ density
σ_k a constant in the k equation
σ_ε a constant in the ε equation
τ shear stress tensors.

Subscripts

aw adiabatic wall
C coolant
i, j cyclical indices
norm normalized values
t turbulent quantity.

1. Introduction

The continuous improvement in the performance of air-breathing propulsion systems necessitates a continuous increase in the turbine inlet temperatures. This, coupled with the demands of reduced size of the combustors, has put a significant burden on turbine technology. Since the inlet temperatures of present generation gas turbines are much higher than the melting temperatures of the available alloys used to make the turbine blades, cooling of the blades is a critical issue in turbine technology. Film cooling, wherein cooler air from the

* Corresponding author. Tel.: 001 352 392 0967; fax: 001 352 392 7303

0017–9310/99/$ - see front matter
PII: S0017–9310(98)00124–0

compressor injected near the blade surface (through holes or slots) to provide a layer of cool fluid between the hot gases and the blade surface, has been an effective approach for this purpose. The design practice in the heat transfer community for film cooling has been mostly empirical in nature, relying heavily on a large experimental database. However, there are many parameters and factors that need to be considered, including inlet Mach number, freestream turbulence intensity, coolant-to-freestream blowing ratio, coolant-to-freestream density ratio, hole shape, size, location, blade shape and spanwise characteristics, etc. Thus, a CFD-based predictive capability to provide detailed fluid dynamic and heat transfer information for given flow parameters is highly desirable. However, before CFD can become a routine design tool for such challenging problems, it must be extensively validated against the existing database as well as carefully designed experiments. The primary limiting factors of CFD for such tasks stem from the lack of comprehensive turbulence models and grid resolution for complex, three-dimensional flow fields. In this work, a systematic effort is made to assess the capability of CFD for such applications by employing a state-of-the-art method and grids with varying resolutions.

Many researchers have investigated the film coolant behavior and its interaction with the hot freestream. Goldstein [1] provides a review of film cooling technology up to 1971; a more recent review is the one by Simoneau and Simon [2]. Many experimental studies have been conducted to study the influence of parameters such as coolant-to-freestream blowing ratio, density ratio, freestream turbulence intensity, etc.; for example, see Sinha et al. [3, 4], Pietrzyk et al. [5], Jumper et al. [6], Salcudean et al. [7], etc. However, many of these studies have been confined to simple geometries such as flat and mildly curved plates (with one or more rows of cooling holes) in steady, incompressible flow. Several computational studies have also been reported. These range from the resolution of detailed flow physics within the coolant holes, e.g., Leylek and Zerkle [8] to solution of a real turbine blade geometry with multiple rows of holes, e.g., Garg and Gaugler [9]. The former uses a flat plate geometry and can be viewed as a step toward developing computational predictive capabilities for realistic geometries and flow situations. The latter uses turbulent profiles (1/7th power law) for the coolant velocity and temperature distribution at the hole exit as boundary conditions and thus does not accurately account for the variation of flow physics within the holes depending on various flow and geometric parameters. Different researchers have employed different turbulence models with varying degrees of success; e.g., Garg and Gaugler [10] have used an algebraic model whereas Amer et al. [11] and Garg and Ameri [12] compare various two-equation models for film cooling flows.

In the present work, a geometry more representative of a turbine leading edge than a flat plate is chosen, for which experimental data is provided by Cruse et al. [13] of the University of Texas, Austin. The geometrical features and flow conditions such as the shape of the leading edge, shape and size of the cooling holes, the length-to-diameter of the coolant ducts (leading from the plenum to the turbine blade surface) coolant-to-freestream density ratio, coolant-to-freestream blowing ratio, etc., are designed to simulate the essential physics associated with a real film-cooled turbine blade leading edge. In the computation, no assumption is made about the flow exiting the cooling holes; instead, the flow within the holes is resolved as a part of the computational procedure by specifying the coolant mass flux in the plenum. The two-equation k–ε turbulence model, with wall functions and low-Reynolds number modifications, is employed. In order to assess the performance of the more widely used versions of the k–ε model, no attempt is made to assess corrections which account for known deficiencies in standard two-equation models such as anisotropy, non-equilibrium, streamline curvature, etc. Computations simulating this experiment have also been conducted by Lin et al. [14] and Martin and Thole [15] who use the k–ω model and the k–ε model with wall functions, respectively. The present work is an extension of a previous work by the same authors [16].

From the designer's point of view, the objective of the film cooling system is to cool the blade effectively with minimal coolant injection and minimum interference with the main flow aerodynamics. The challenge for pragmatic CFD applications is to accurately predict key features of the flow with reasonable computing resources and turn-around times. To help develop such a computational tool for advanced film cooling design concepts, the CFD capability must first be validated against available experimental data, using a combination of reasonable grid size for engineering analysis, practical turbulence models and a realistic geometric definition. Our view is that in order to facilitate a routine use of a CFD capability in the design process, it needs to be able to do the following:

(1) provide solutions in a reasonable time (about a day or so on a high-performance workstation)
(2) allow changes, in a reasonable time, in geometric definitions for parametric assessment, and
(3) be streamlined enough to offer not only the key information required in the design process, such as cooling effectiveness, but also physical insight into the flowfield and heat transfer characteristics.

The above factors have guided the computational approach presented here. In the following, we will first outline the key features of the CFD solver employed in the present study (Shyy [18], Thakur et al. [17]). After that we present the computational results for the leading

edge film cooling problem and compare them to the experimental data. This is followed by an examination of the flow field and a description of the flow physics. Finally, a preliminary parametric study, involving the variation of two geometric parameters, is presented to demonstrate the usefulness of a CFD capability for optimization purposes.

2. The flow solver

2.1. Algorithm

We use a pressure-based flow solver which employs structured body-fitted grids for simulating steady compressible/incompressible, laminar/turbulent flows. Various convection schemes including first-order upwind, second-order upwind, central difference and a TVD-based controlled variation scheme (CVS) are implemented in the code (Thakur et al. [19]). The flow solver is based on the SIMPLE (Semi-Implicit Method for Pressure-Linked Equations) algorithm (in Cartesian coordinates see Patankar [20]; for extension to curvilinear coordinates, see Shyy [18]). The implementation employs a control volume approach and uses a staggered grid for the velocity components and the scalar variables like pressure, in order to handle the open-domain pressure boundary condition in a manner consistent with the mathematical formulation of the governing equations. One of the main features of our approach is a mixed Cartesian-contravariant velocity component formulation. Such an approach eases the handling of the conservation of linear momentum and the mass continuity constraint effectively in curvilinear coordinates. The Cartesian velocity components are computed from the respective momentum equations. The contravariant velocity and pressure fields are corrected using a pressure correction equation which is derived by manipulating the continuity and the momentum equations. Then the Cartesian velocity components are updated via the Dyakonov iteration procedure. The correction procedure leads to a continuity-satisfying velocity field. The whole process is repeated until the desired convergence is reached. Details can be found in Shyy [18]. For development of this algorithm in a multi-block framework, see Thakur et al. [17]. All these aspects have been incorporated into a general-purpose CFD code named SEAL.

Employing indicial notation, the continuity, momentum and energy equations can be written as follows:

$$\frac{\partial \varrho}{\partial t} + \frac{\partial}{\partial x_j}(\varrho u_j) = 0 \tag{1}$$

$$\frac{\partial}{\partial t}(\varrho u_i) + \frac{\partial}{\partial x_j}(\varrho u_j u_i) = -\frac{\partial p}{\partial x_i} + \frac{\partial \tau_{ij}}{\partial x_{ij}} \tag{2}$$

$$\frac{\partial}{\partial t}(\varrho H - p) + \frac{\partial}{\partial x_j}(\varrho u_k H) = -\frac{\partial q_j}{\partial x_i} + \frac{\partial}{\partial x_j}(u_i \tau_{ij}) \tag{3}$$

The instantaneous form of the above equations for turbulent flows is obtained by time-averaging. Favre-averaging is used for velocity components and temperatures, and Reynolds-averaging is used for density and pressure. Finally, after incorporating the standard modeling assumptions for averaged fluctuating quantities, the Navier–Stokes equations are cast in a generalized body-fitted coordinate system, (ξ, η, ζ), which can be found in Shyy [18].

2.2. The standard k–ε model with wall functions

One of the turbulence models employed is the standard k–ε model (Jones and Launder [21], Launder and Spalding [22]), which is widely used for engineering applications. The velocity, k and ε at the first node near a solid wall are obtained using wall functions which are based on the assumption that the boundary layer structure near any solid wall is similar to that of a flat plate boundary layer and that turbulence is in local equilibrium (production of turbulent kinetic energy equals its dissipation). The eddy viscosity is estimated from the following:

$$\mu_t = \frac{C_\mu \varrho k^2}{\varepsilon} \tag{4}$$

where C_μ is a proportionality constant (0.09). For a detailed description of the implementation of wall functions in body-fitted coordinates, the reader is referred to Thakur et al. [17].

2.3. Low-Reynolds number k–ε model

The low-Reynolds number models integrate the governing equations all the way to the wall and thus obviate the need to make any assumptions about the nature of turbulence or the velocity profile near solid walls. The model we have used here is the one proposed by Nagano and Tagawa [23]. Although there are numerous low-Reynolds number models available in the literature, we have chosen this particular model since it has been tested for boundary layer flows with heat transfer [Youssef et al. [24]). This model has been shown to accurately predict the near-wall limiting behavior of turbulence and the effect of adverse pressure gradient on shear layers. It has been validated for various kinds of wall turbulent shear flows, e.g., a pipe flow, a flat-plate boundary layer, a diffuser flow, a relaminarizing flow, etc. (Nagano and Tagawa [23]). Also, Youssef et al. [24] have used this model in conjunction with a two-equation model for heat transfer (which models the transport equations for the variance of temperature and its dissipation rate), and have reported satisfactory results for heat transfer in

turbulent boundary layers with different types of wall thermal conditions. The model can be summarized as follows:

$$\mu_t = \frac{C_\mu f_\mu \varrho k^2}{\varepsilon} \tag{5}$$

$$\frac{D(\varrho k)}{Dt} = \frac{\partial}{\partial x_i}\left[\left(\mu + \frac{\mu_t}{\sigma_k}\right)\frac{\partial k}{\partial x_i}\right] + P - \varrho\varepsilon \tag{6}$$

$$\frac{D(\varrho \varepsilon)}{Dt} = \frac{\partial}{\partial x_i}\left[\left(\mu + \frac{\mu_t}{\sigma_\varepsilon}\right)\frac{\partial k}{\partial x_i}\right] + C_1 f_1 P\frac{\varepsilon}{k} - C_2 f_2 \varrho\frac{\varepsilon^2}{k} \tag{7}$$

$$f_2 = \left[1 - 0.3\ \exp\left\{-\left(\frac{Re_t}{6.5}\right)^2\right\}\right]\cdot\left[1 - \exp\left(-\frac{y^+}{6}\right)\right]^2$$

$$f_\mu = \left[1 - \exp\left(-\frac{y^+}{26}\right)\right]^2\cdot\left[1 + \frac{4.1}{Re_t^{3/4}}\right]$$

$$P = \mu_t\frac{\partial u_j}{\partial x_i}\left[\frac{\partial u_j}{\partial x_i} + \frac{\partial u_i}{\partial x_j}\right] \quad Re_t = \frac{\varrho k^2}{\mu\varepsilon}$$

$$C_\mu = 0.09 \quad C_1 = 1.45 \quad C_2 = 1.9 \quad f_1 = 1.0$$
$$\sigma_k = 1.4 \quad \sigma_\varepsilon = 1.3 \tag{8}$$

Boundary conditions at a solid wall:

$$k = \frac{\partial k}{\partial y} = 0, \quad \varepsilon = 2\frac{\mu}{\varrho}\left(\frac{\partial\sqrt{k}}{\partial y}\right)_w^2 \tag{9}$$

3. Problem description

3.1. Experimental geometry and boundary conditions

The experiment conducted by Cruse et al. [13] uses a polystyrene model with a cylindrical leading edge of radius 50.8 mm, representing the leading edge of a real turbine blade. A schematic of the experimental setup is shown in Fig. 1, where the coordinate system used is such that the x-axis is along the direction of the freestream, y-axis is normal to the walls of the wind tunnel and the z-axis is along the span of the blade surface, as shown in Fig. 1(a). The polystyrene model is placed in the wind tunnel with a $0.15\times0.6\times1.8$ m test section, with hot freestream gases approaching the model from left to right. As shown in Fig. 1(a), a half leading edge is simulated by using a suction slot to position the stagnation line at the appropriate location. The model surface has two rows of holes leading into a plenum chamber through which air, cooled to 166 K using liquid nitrogen, is injected. Each row consists of nine holes (each with a diameter $D = 6.32$ mm) with an injection angle of 20° to the lateral direction as shown in Fig. 1(b). The first (bottom) row of holes is located at the stagnation line position (symmetry plane of the leading edge for the computations) and the second (top) row is located a few hole diameters downstream (at an angle of 25° relative to the first row). The surface of the model is hydrodynamically smooth (roughness less than 25 μm). Also, the conduction errors at the model surface are small and it is assumed adiabatic [13]. The freestream (hot) velocity magnitude is 10 ms^{-1} and the freestream temperature is 27°C. The turbulence intensity of the freestream flow is 0.5%. The density ratio between the coolant and the freestream is 1.8 and the overall blowing ratio (defined as $\varrho_C U_C/\varrho_\infty U_\infty$, where subscript C represents the coolant and ∞ the freestream, and U_C is the average velocity of the coolant coming out of the holes) is 2.0.

3.2. Computational domain and grids used

The computational domain is depicted in Fig. 1(d). The plenum is truncated as shown, with the two side boundaries treated as slip walls. Only one pair of top–bottom holes is considered for the computation assuming periodicity of flow between neighboring pairs of holes, as shown in Fig. 1(c) and (d). The computational domain is divided into four blocks—one in the plenum, one each in the two coolant ducts (leading from the plenum to the blade surface) and one in the outer domain, as depicted in Fig. 2(a). The experimental conditions are controlled (using the suction flow shown in Fig. 1(a)) such that the stagnation streamline lies in the horizontal plane through the center of the bottom row of holes [13]. Thus, that plane is treated as a symmetry plane in the computational domain; see Fig. 1(a) and (d). The entire first-row hole, from the plenum to the blade surface, is modelled. The symmetry condition is enforced by assigning the flowfield information on the bottom half of the exit plane of this hole (i.e., the plane of intersection of Block 2 and Block 4 in Fig. 2(a)), along with the region below the symmetry plane in Block 4, from above the symmetry plane (at every iteration of the solution procedure). At the plenum entrance, the coolant mass flux is specified. In the experiment, the coolant mass flux in the plenum is 13.05 g/s. In the computation, we specify a coolant mass flux of 1.45 g/s (for one pair of top-bottom holes) by assigning a plug profile for velocity at the plenum entrance (Fig. 1(d)).

As the first case, a coarser grid (not shown here) consisting of $27\times101\times41$ nodes in the outer domain (Block 4) was used, without near-wall clustering, employing wall function treatment. The details of the results obtained on this grid are not presented here; however, we note here that the use of wall functions for this problem, with its complex physics near the solid walls, accompanied by the inadequate grid resolution of this grid, clearly illustrated the need for both improved near-wall turbulence model and an increased grid resolution. Nevertheless, this computation provided a good initial guess for the subsequent computations conducted on the three successively refined

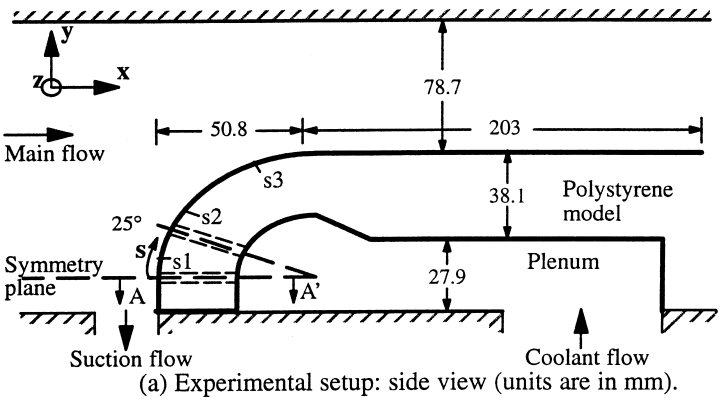

(a) Experimental setup: side view (units are in mm).

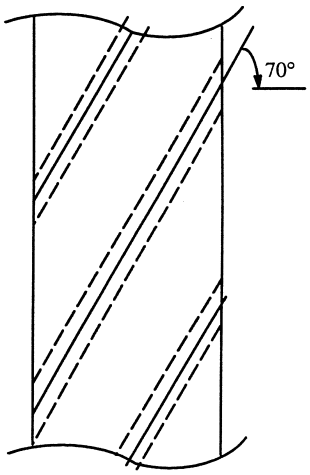

(b) Section A–A' from (a).

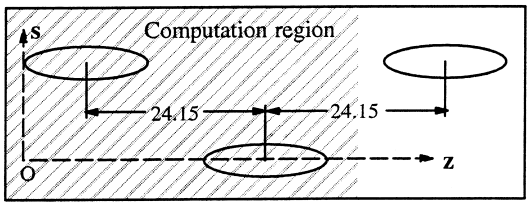

(c) Front view of the leading edge.

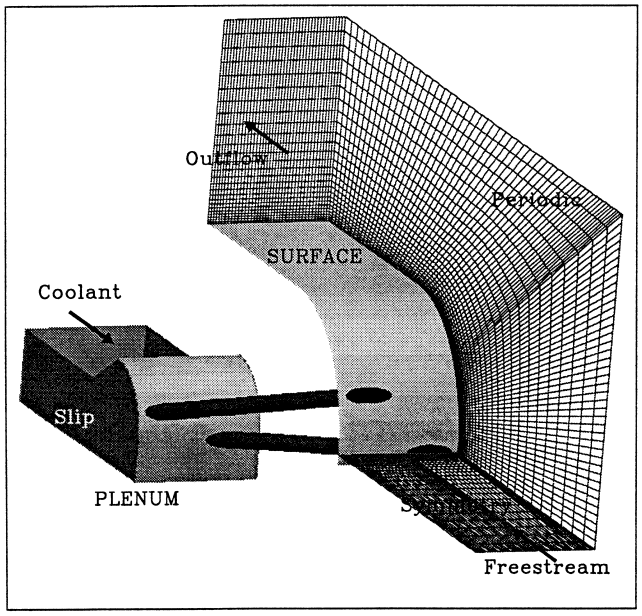

Fig. 1. Illustration of experimental geometry and computational domain.

grids shown in Fig. 2, for which the low-Reynolds number version of the k–ε model is employed. For facilitating discussion, these grids are labelled as follows:

(a) COARSE ($37 \times 101 \times 61$ nodes in the outer block; approx. 0.25×10^6 in the whole domain)
(b) MEDIUM ($67 \times 101 \times 61$; 0.5×10^6 total) and
(c) FINE ($67 \times 111 \times 121$; 10^6 total).

These grids differ mainly in the distribution of nodes near the leading edge, especially in the region of interaction of the coolant jets issuing from the holes and the freestream fluid. Compared to the first grid which employed wall functions, the COARSE grid contains additional points near the wall for the low-Reynolds number model. The MEDIUM grid further refines the grid in the stagnation region and the region of interaction of the freestream

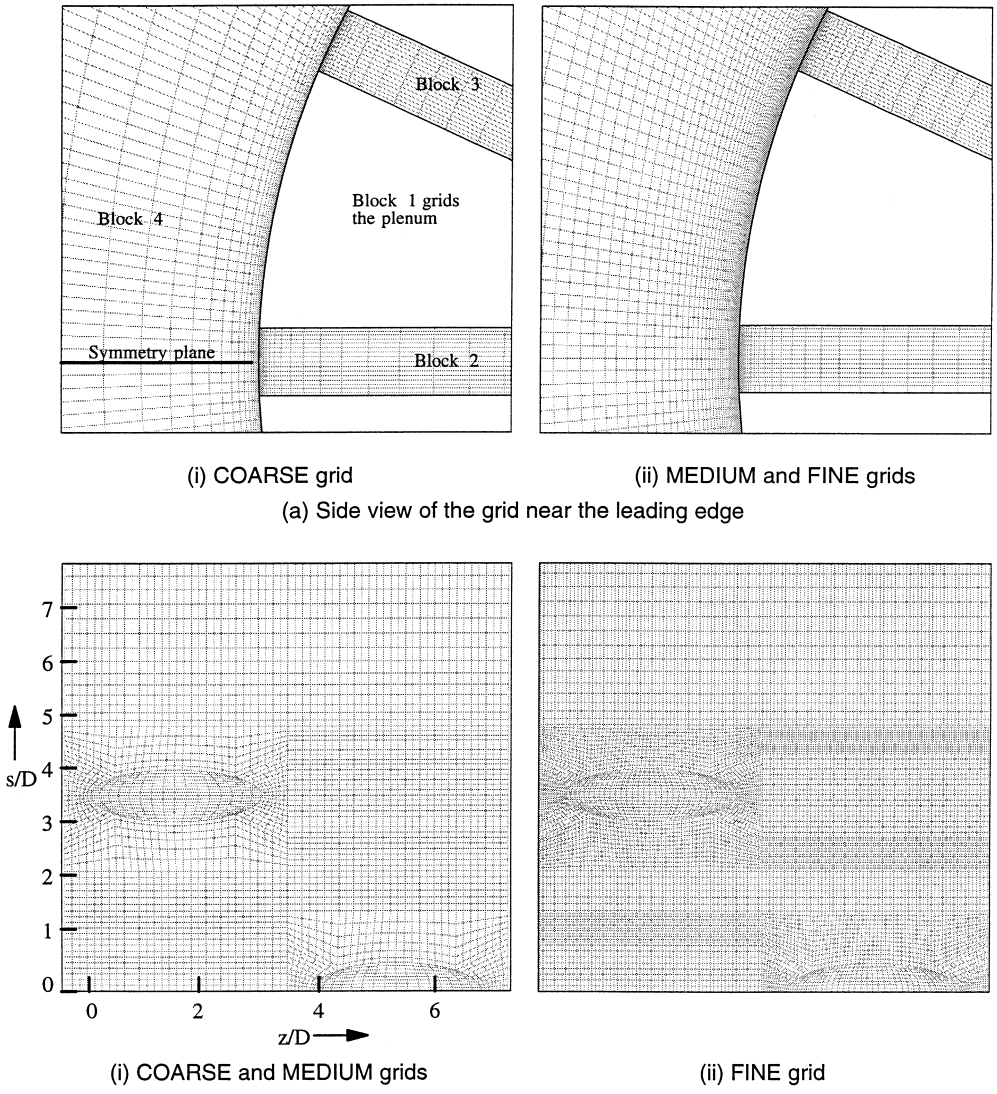

Fig. 2. Node distributions for the COARSE, MEDIUM and FINE grids.

with the coolant jets (Fig. 2(a)). Finally, the FINE grid is constructed by doubling the number of nodes of the MEDIUM grid in the lateral (z) direction (Fig. 2(b)). For the fine grid, the first computational node was ensured to be within the laminar sublayer, with the y^+ value less than 1.0, all along the blade surface. A summary of these grids is provided in Table 1.

4. Computational results

One of the objectives of the present work has been to investigate the predictive capabilities of the present CFD algorithm with an intent of incorporating it in the gas turbine design process and heat transfer analysis. This necessitates the judicious use of computational tools including grid distribution, discretization schemes, etc. It is desirable to use a combination of efficient grid distribution to capture key physics in regions of the flow domain which dictate the overall nature of the entire flowfield, as well as a high-order discretization scheme to predict solutions with a reasonable degree of accuracy. For the present computations, a second-order controlled variation scheme (CVS), which is formulated using a TVD-based second-order upwinding [17, 19], is employed to discretize the governing equations. Three different grid systems are used, as discussed in the previous section. The low-Reynolds number k–ε model discussed in Section 2.3

Table 1
Summary of the computational cases

Case	Grid name	Outer block grid size	Wall treatment in outer block	Mass-split (top–bottom hole)
1	–	$27 \times 101 \times 41$	Wall functions	0.502–0.498
2.	COARSE	$37 \times 101 \times 61$ (clustering near surface)	Low-Reynolds number model	0.52–0.48
3	MEDIUM	$67 \times 101 \times 61$ (clustering near surface & in stagnation region)	Low-Reynolds number model	0.52–0.48
4	FINE	$67 \times 111 \times 121$ (clustering near surface & in stagnation region + doubling of nodes in z-direction)	Low-Reynolds number model	0.52–0.48

is used for turbulence closure in the main flow domain (Block 4), whereas wall functions are used within the two holes (Blocks 2 and 3). For the temperature field, a constant turbulent Prandtl number (0.9) is assumed. To start the computation, the freestream conditions are specified in the entire outer domain (Block 4) and the plenum inlet conditions are specified in the entire plenum (Block 1) and the two holes (Block 2 and 3). First, a converged solution is obtained on the COARSE grid. This solution is interpolated on to the MEDIUM grid to serve as an initial guess and subsequently the MEDIUM grid solution is interpolated to yield an initial guess for the FINE grid. Though this procedure is not necessary to yield a converged solution on the finer grids, it substantially speeds up the computational process.

4.1. Comparison of computations with experiment

The experimental data is provided in the form of adiabatic cooling effectiveness, η, which is defined as

$$\eta = \frac{T_{aw} - T_\infty}{T_C - T_\infty} \tag{10}$$

where T_{aw} is the adiabatic wall temperature. The data is provided in the form of point values on the blade surface using a rectangular grid mapped on to it. Spanwise-averaged η and profiles of η at three streamwise locations are extracted from this surface data (for both the experiment and the computation) and are shown in Fig. 3. Another non-dimensional quantity used to examine the thermal field is the normalized temperature which is defined as follows:

$$T_{norm} = \frac{T - T_\infty}{T_C - T_\infty} \tag{11}$$

Note that on the blade surface, the normalized temperature is identical to the adiabatic effectiveness. The contours of normalized temperature on the blade surface are plotted in Fig. 4, where blue represents the coolant temperature and red represents the (hot) freestream temperature.

It should be noted that though periodicity is assumed in the lateral direction in the computation (Fig. 1), the experimental data provided reveals that periodicity is not strictly achieved in the experiment. This is evident from the normalized surface temperature distribution shown in Fig. 4 and the profiles of adiabatic effectiveness shown in Fig. 3. For example, just downstream of the first row of holes (Fig. 3(b)), the experimentally measured η profiles show a higher peak near the left hole than the right hole; just downstream of the second row of holes (Fig. 3(c)), the measured η profiles show a higher peak near the right hole than the left hole. It should also be mentioned here that the resolution of the infrared camera used to measure the surface temperature is $0.43\ D \times 0.43\ D$, which implies that the experimental value at any point is the average over an area equal to $0.43\ D \times 0.43\ D$.

4.1.1. Spanwise-averaged adiabatic effectiveness

Figure 3 shows the plots of laterally averaged η versus the streamwise coordinate (s/D) as well as the profiles of η vs the spanwise coordinate (z/D) on the blade surface at three streamwise locations. Here s is the streamwise coordinate along the surface of the blade starting at the symmetry plane (center of the bottom hole) as shown in Fig. 1(a) and D is the diameter of the holes. From Fig. 3(a), it can be seen that the computations predict the correct trend for the laterally averaged η. The adiabatic effectiveness is high at the leading edge, decreases as one proceeds downstream on the blade surface, increases just downstream of the top row of holes and then decreases again as we go further downstream. The predicted values of η are higher than the experimental data as we proceed downstream. It is also evident from Fig. 3(a) that the

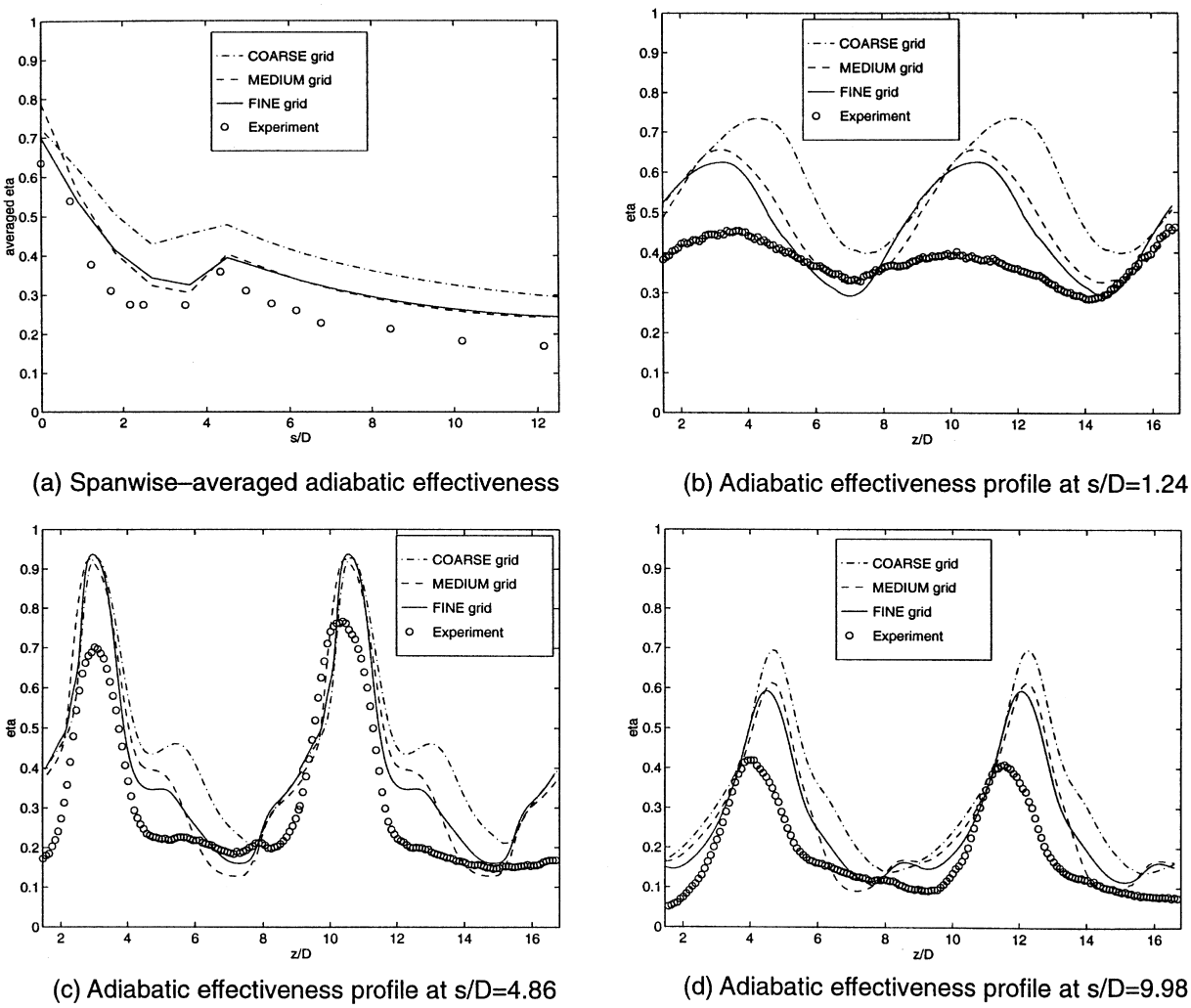

Fig. 3. Spanwise-averaged and profiles of adiabatic effectiveness at three streamwise locations.

prediction of the average surface temperature distribution improves progressively as one refines the grid.

4.1.2. Profiles and contours of adiabatic effectiveness

The spanwise η profiles are plotted at three s/D locations:

(a) $s/D = 1.24$ (located just downstream of the bottom row of holes; $s1$ in Fig. 1(a))
(b) $s/D = 4.86$ (located just downstream of the top row of holes; $s2$ in Fig. 1(a)), and
(c) $s/D = 9.98$ (far downstream from the hole locations; $s3$ in Fig. 1(a)).

The computations predict higher levels of surface adiabatic effectiveness compared to the experimental data at all three locations, although the trend is consistent with the experimental data. The η profile predicted by the computation matches the experimental profile reasonably well in terms of the location of the maximum and the minimum values. As mentioned earlier, the experimental data is not exactly periodic in its hole-to-hole variation. Comparing the COARSE and the FINE grid computations, there is an obvious improvement in the prediction of the profiles as the grid is refined in the stagnation region. This indicates that an adequate resolution of the regions of interaction of the coolant jets and the free-stream fluid is essential to predict the correct mixing (of the coolant and the mainstream) and the entrainment (of the main fluid into the jet cores) which in turn is necessary to obtain the correct penetration of the coolant jets and their spreading rates. On the other hand, the differences between the solutions on the MEDIUM and FINE grids are small, indicating that the discrepancies between the numerical and experimental results are likely to be affec-

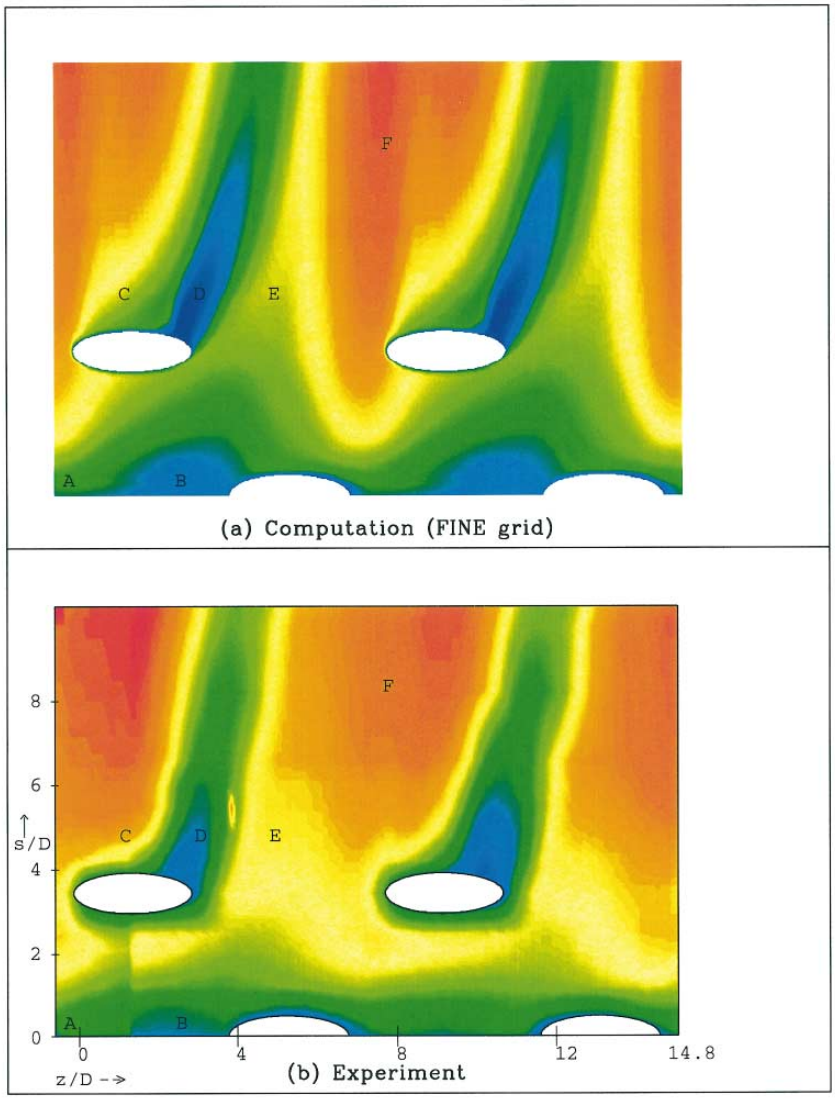

Fig. 4. Normalized surface temperature contours.

ted by other factors such as the turbulence model employed.

Figure 4 shows the contour plots of normalized temperature on the blade surface from the experiment and the computation on the FINE grid. The lower temperatures (higher levels of η) near the leading edge and immediately downstream (and to the right) of the top hole are due to the interaction between the coolant jets and the free-stream, as discussed in more detail in the next section. These features in the computed results agree reasonably well with the experimental data, though the levels of cooling are, on an average, higher than the experimental data. This is consistent with the profiles of η as discussed above.

Finally, it should be noted that the plot of spanwise averaged adiabatic effectiveness shows a better agreement with the data than do the spanwise profiles. There are significant differences between the computation and the experiment in the magnitudes of surface temperature as evident from the profile plots of Fig. 3 but the averaging of information across the span of the blade tends to obscure this fact. This indicates that caution must be exercised when interpreting averaged data.

4.2. Flow field

To aid the description of key features of the flowfield, it is helpful to consider the following interactions sep-

arately: interaction between the bottom jets (first row holes) and the freestream, interaction between the top jets (second row holes) and the freestream, and interaction between the bottom and top jets. To illustrate these interactions, streamlines near the leading edge of the blade are plotted in Fig. 5. The streamlines in Fig. 5 (top) are seeded in the symmetry plane a short distance upstream of the leading edge as well as at the exit plane of the bottom hole and show the interaction between the freestream and the bottom coolant jet. The streamlines in Fig. 5 (bottom) are seeded at the exit plane of the two holes and show the interaction between the coolant jets from the bottom and top holes.

As it approaches the leading edge near the symmetry plane, the freestream acquires a strong lateral (z) component due to the bottom cooling jets. This leads to a much smaller crossflow velocity and a higher pressure upstream of the bottom holes compared to the top holes where there is a strong crossflow due to the acceleration of the freestream over the curved surface of the blade. There is a region of recirculation (marked A in Fig. 5) where hot freestream mixed with the coolant produces

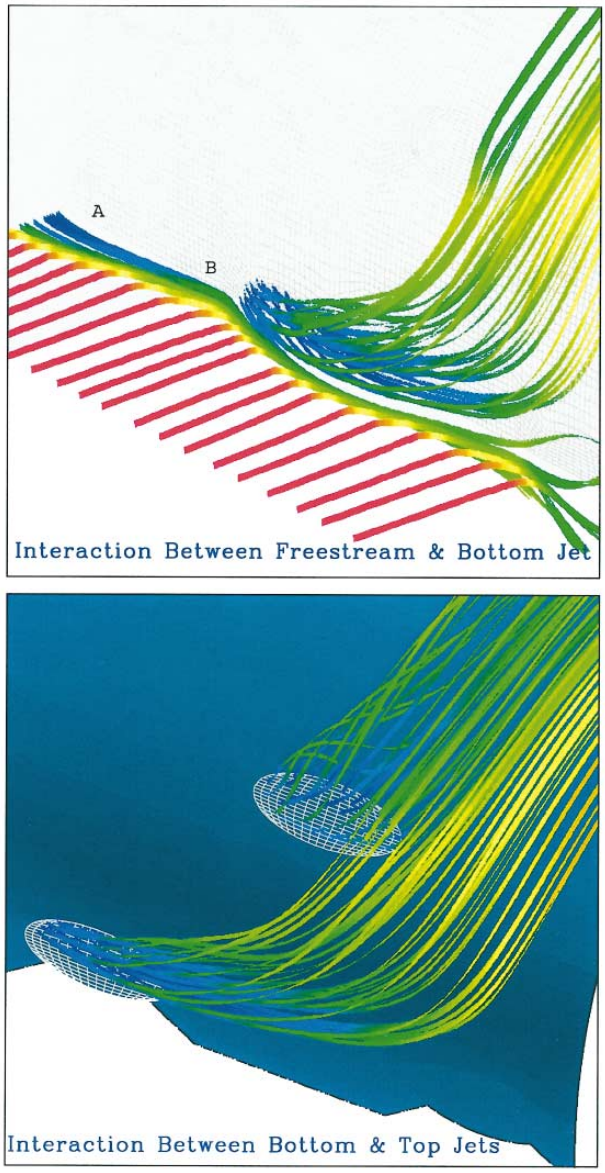

Fig. 5. Streamlines illustrating freestream-coolant interaction.

slightly higher surface temperatures compared to the surrounding areas. The trajectory of the jet upstream of the region marked 'A' in Fig. 5 (blue represents the coolant temperature) indicates that the coolant is directed towards the surface of the blade by the freestream, just past the region of recirculation. This region is labelled 'B' and lies just to the left of the bottom hole. The corresponding region of low temperature (and hence high adiabatic effectiveness) is also labelled 'B' in Fig. 4. Another important feature of the flow near the symmetry plane is the formation of vortices due to the strong lateral component of the freestream and the outward flow of the coolant. This can be observed in the velocity vectors projected on to XY planes near the symmetry plane shown in Fig. 6. These planes are located at four spanwise stations normal to the blade surface near the first-row hole as shown at the bottom of Fig. 6. The vectors in Fig. 6 are colored according to temperature, blue representing the coolant temperature and red the freestream. These vortices increase in strength as one goes away from the bottom hole in the spanwise direction (XY planes 1 and 2) and then decrease (XY planes 3 and 4). It can be observed that due to the formation of these vortices, the hot freestream gases are able to get behind the coolant jets, thus heating the surface. This can be observed most clearly in XY planes 2 and 3 where the mixing of the freestream with the coolant (in the form of green and light blue vectors adjacent to the blade surface) behind the coolant jet (dark blue vectors) can be seen.

The interaction between the freestream and the coolant jet from the top hole is significantly different from that with the bottom jet due to strong crossflow across the top hole owing to the acceleration of the flow over the curved leading edge. The pressure drop between the second-row hole and the plenum is higher than that between the first-row and the plenum due to the stagnation region upstream of the first-row holes. This causes a slightly higher mass flow rate (52%) through the second-row holes than the first-row holes (48%) as noted in Table 1, which implies that the coolant-to-freestream mass flux ratio is slightly less than 2.0 for the first-row holes and slightly higher than 2.0 for the second-row holes. The strong crossflow over the second-row (top) hole leads to an increase in the jet speed in the bottom half of the jet. The jet issuing from the left portion of the coolant top hole lifts off and interacts with the freestream to generate a vortex which entrains the hot gas and pushes it near the blade surface. Compared to the bottom hole, the coolant is swept downstream with significantly less lateral spreading of the jet.

A portion of the jet from the bottom hole mixes with the freestream and essentially flows in a spanwise direction to provide cooling to the leading edge region. The remainder of the jet gets swept downstream. The path taken by the bottom jet downstream can be seen in Fig. 5(a). A portion of the bottom jet flows directly over a portion of the top jet. This interaction between the bottom and top jets immediately downstream and to the right of the top hole causes cool fluid to be swept down towards the blade surface, thus causing a high level of cooling in that region, marked 'D' in Fig. 4, of the blade surface. The bottom jet thus serves to shield a portion of the top jet from the freestream and prevents it from penetrating deeper into the freestream.

4.3. Thermal field

In the vicinity of the bottom row of holes, there is a relatively uniform spanwise variation of adiabatic effectiveness. This is due to the fact that the bottom cooling jets spread much more in the lateral direction than in the normal direction. Though the computation predicts the same trend as the experiment, it under-predicts the lateral spreading of the jets and over-predicts the normal spreading ;this can be attributed to the turbulence model which does not account for anisotropy. It can also be noted from Fig. 4 that there are regions between the holes in the bottom row (specially, immediately to the right and downstream of a bottom hole) where surface temperature is high compared the neighboring regions on the symmetry plane where it is low (specifically, to the immediate left of a bottom hole). The former (regions marked 'A') are due to the vortices which cause the hot freestream to be entrained towards the blade surface by the cooling jets and the latter (regions marked 'B') are due to the coolant jets being pushed back to the surface by the freestream. Overall, the entrainment of the freestream at the leading edge is the reason for some heating at the leading edge as also evident from the spanwise averaged η and the η profile at the location $s/D = 1.24$ (Fig. 3).

The coolant from the top row of holes is swept downstream and undergoes very little lateral spreading due to the strong crossflow velocity of freestream there. Downstream of the top rows of holes, there are narrow bands of low temperature alternating with large regions of high temperature. The former, marked as regions 'D' in Fig. 4 are due to the coolant which is pushed towards the surface because of a portion of the bottom cooling jet which flows directly over the top cooling jet. The latter, marked as regions 'C', 'E' and 'F' in Fig. 4, can be attributed to several factors. First, a portion of the bottom cooling jets flows directly over the top cooling jets indicating a waste of coolant. Second, the bottom jets lift off as they approach the top jets due to the adverse pressure gradients caused by the latter. Thus, since it does not stay attached to the surface, the coolant from the bottom holes fails to effectively cool the surface downstream of the holes in the top row as evident from the large surface area which is essentially uncooled (region 'F' in Fig. 4). Third, the freestream-jet interaction causes a lift-off of the top cooling jet leading to an entrainment of hot gas under the jet as can be seen from the streamlines eman-

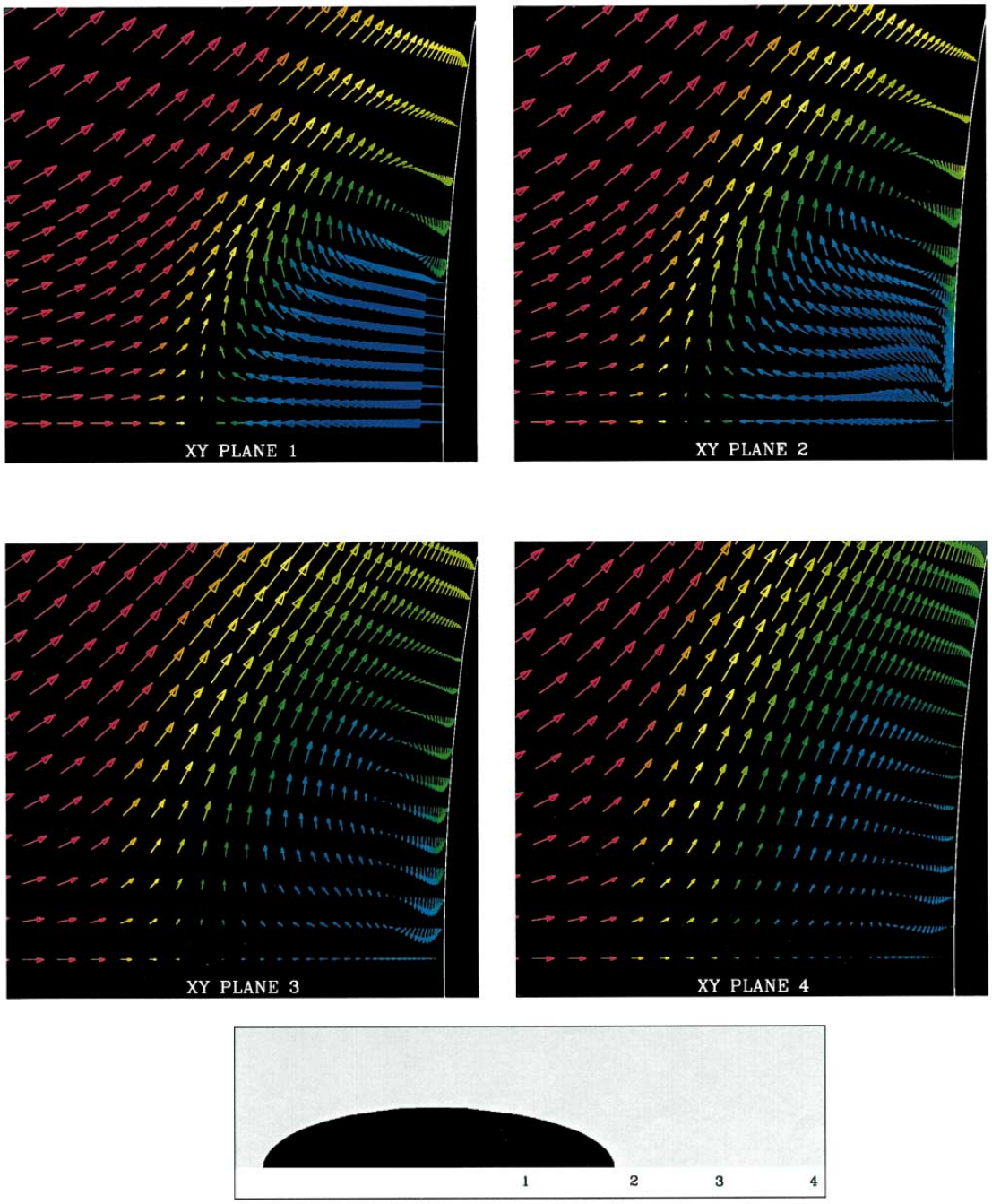

Fig. 6. Velocity vectors projected on to *XY* planes at the leading edge. Locations of the planes are shown at the bottom of the figure.

ating from the left half of the second-row hole shown in Fig. 5 (bottom). This causes a high temperature (low effectiveness) immediately downstream of the left half of the top holes, marked as region 'C' in Fig. 4. It should also be noted that the computation predicts a slight cooling from the bottom jet as far downstream as the second-row of holes, as shown by region 'E' in Fig. 4(a), whereas the extent of the influence of the bottom jet observed in the experiment is lesser (the corresponding region 'E' in Fig. 4(b) is essentially uncooled).

Figure 7 shows contours, at three streamwise locations, on planes normal to the blade surface and extending into

(a) s/D=1.24

(b) s/D=4.86

(c) s/D=9.98

Fig. 7. Non-dimensional temperature contours on planes normal to the surface.

the freestream, of normalized temperature and serves to illustrate the penetration and the spread of the bottom and top jets, as predicted by the computation. The entrainment of the hot freestream gas by the coolant jets can be clearly observed. The top coolant jets entrain significantly larger amounts of hot freestream gas than the bottom coolant jets due to the larger mainstream crossflow, as mentioned earlier. Also, the vortex rolls up to the left whereas the jet itself moves to the right as it penetrates downstream, as seen in Fig. 7(b) and (c). Large regions, which increase in size downstream, of essentially uncooled surface between the holes in the top row can also be observed.

5. Parametric variation

In this section, we present the results of a preliminary parametric variation study aimed at demonstrating the potential of CFD for optimization. There are numerous flow and geometric parameters that one can choose to optimize. Among the flow parameters are the coolant-to-freestream blowing ratio, coolant-to-freestream density ratio, etc. Geometric parameters that one might choose to optimize include lateral spacing of the holes (pitch), shape of the holes, coolant injection angle, relative stagger between the rows of holes, relative angle between the holes, etc. Depending on the number of parameters chosen, a multi-dimensional response-surface based optimization can be conducted. The objective functions that can be used include maximum surface temperature, percentage of surface area above a specified cutoff temperature, uniformity of surface temperature distribution, etc. We have chosen, for demonstrating the viability of CFD for optimization purposes, two geometric parameters, i.e.,

(a) the relative angle between the first and the second row of holes
(b) the relative stagger between the first and the second row of holes.

The relative angle between the two rows of holes is

defined as the angle between the lines drawn radially outward from the center of the cylindrical leading edge surface along the center of the holes, as viewed along the lateral (z) direction. Three angles are used: 20°, 25° and 30°. The relative stagger between the two rows is defined based on the lateral location of a bottom hole relative to the two top holes (which are fixed), as viewed along the streamwise (x) direction. The 'baseline stagger' geometry is the one where the center of the bottom hole is located midway between the centers of two successive holes in the top row. The geometry with the bottom hole located one-sixth of the hole-to-hole distance to the left relative to the 'baseline stagger' case is labelled 'left stagger' and the one with the bottom hole an equal distance to the right is labelled 'right stagger'. These definitions are illustrated in Fig. 8. The combination of these two parametric variations leads to a total of nine cases. Note that the case with 25° relative angle and 'baseline stagger' is the experimental geometry which has been used for the computations discussed in the paper so far and is labelled as the BASELINE case. It should be noted that though the MEDIUM and FINE grids yield successive improvements in the baseline solution (as seen from Fig. 3), the COARSE grid captures the essential features of the flow. Thus, grids with resolutions equal to that of the COARSE grid for the baseline case (Fig. 2) are used for the nine cases in the parametric study. An efficient grid generation strategy is utilized wherein patches surrounding and

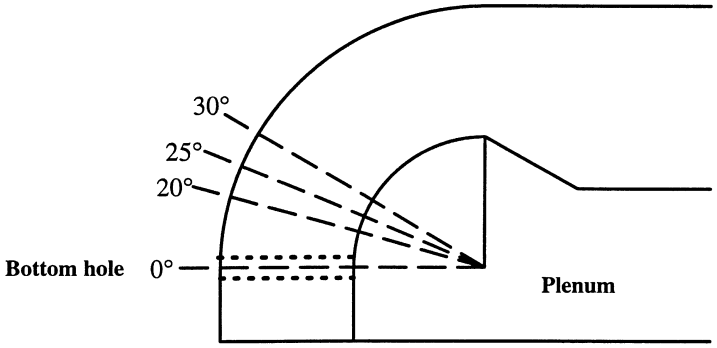

(a) Relative angle between the first (bottom) and the second (top) rows of holes

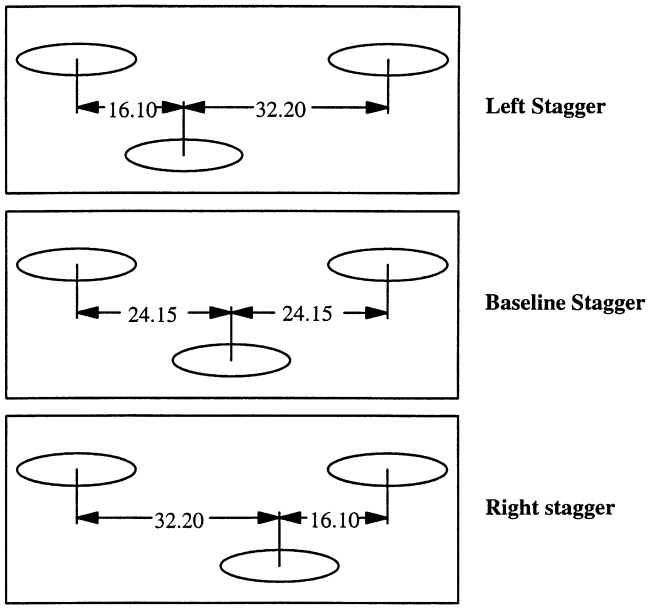

(b) Degree of stagger between the first (bottom) and the second (top) rows of holes

Fig. 8. Geometric parameters: stagger and relative angle between the bottom and top rows of holes.

covering the bottom holes are translated along the blade surface to construct the surface grid for each case, starting from the BASELINE case. Moreover, a similar strategy is used to interpolate the converged solution from the BASELINE case to provide an initial guess for every other case.

Contour plots of adiabatic effectiveness on the surface of the turbine blade for the nine geometries resulting from the combinations of relative angle and relative stagger between rows of holes are shown in Fig. 9. Note that the contours are colored according to the magnitude of adiabatic effectiveness (η); red indicates high η (and thus low temperature) whereas blue indicates low η (high temperature). Detailed quantitative analysis is not presented here but several important qualitative observations can be made. Fig. 9 shows that the degree of stagger has opposing effects in the cooling of the region near the bottom row of holes and the region downstream of the top row of holes. Staggering the bottom holes to the left increases the size of the region of high η downstream of the top holes while decreasing the cooling effectiveness near the bottom holes (i.e. near the symmetry plane). Staggering the bottom hole to the right has an exactly opposite effect. Decreasing the relative angle from the BASELINE case to 20° increases the size of high-effectiveness region downstream and to the immediate right of the top hole, whereas increasing the relative angle has an opposite effect. The surface adiabatic effectiveness distribution appears to be more sensitive to the variation in the relative stagger than that in the relative angle. As can be seen from Fig. 9, the blade surface area covered by the coolant varies depending on the relative angle

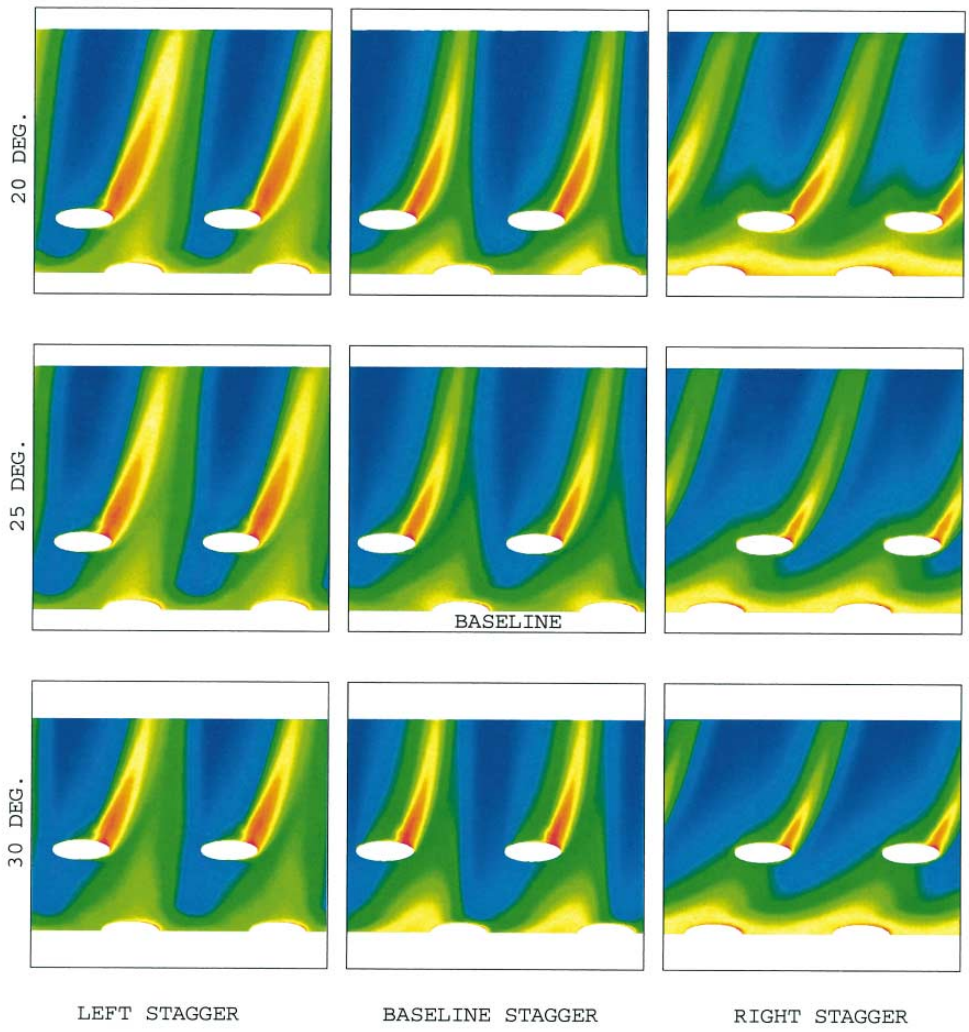

Fig. 9. Contours of adiabatic effectiveness for the parametric variations of the relative stagger and the relative angle for the two rows of holes.

and the relative stagger. For example, by staggering the bottom holes to the right the coolant appears to cover more surface area between the two roles of holes, whereas by staggering to the left the coolant covers more area downstream of the second row. The percentage of surface area exposed to temperatures above a desired value (i.e., the area with η below a specified value) can be used as a quantitative measure of film coverage.

The above results demonstrate the potential for the use of CFD for optimization in film cooling. The moderate size of the grids used for the above parametric study allows fast turn-around times while capturing essential flow and thermal characteristics. The flow and thermal field information thus obtained can be efficiently incorporated in an optimization strategy.

6. Concluding remarks

Computations of a leading edge film cooling flow over an experimental test geometry with two staggered rows of top and bottom holes have been conducted. The coolant flow from the film cooling holes is considered as part of the solution by resolving the flow in the cooling ducts leading from the plenum to the surface of the turbine blade; only the coolant mass flux is specified in the plenum. A systematic grid refinement study is performed and the importance of grid resolution demonstrated. The results show reasonable qualitative agreement with the experimental data which is provided in the form of adiabatic surface film cooling effectiveness. The spanwise averaged adiabatic effectiveness shows a better agreement with the data than does the spanwise variation, indicating that caution must be exercised when interpreting averaged data. Quantitative discrepancies between the computed and experimental results can be attributed, in part, to the isotropic eddy viscosity turbulence model which does not account for the strong anisotropy inherent to the present flowfield. Several key features resulting from the interaction of the cooling jets with the freestream and the interaction of jets from different holes are identified and are used to explain the experimentally observed thermal field. Finally, a preliminary parametric variation study is conducted to demonstrate that CFD can serve as a useful tool for optimization in the design process.

Acknowledgements

This work was conducted under a grant from Pratt & Whitney, West Palm Beach, Florida. The authors would like to acknowledge Martin Tabitta, Fred Soechting and Dean Johnston of Pratt & Whitney for helpful discussions, as well as David Bogard of University of Texas at Austin who provided the experimental data.

References

[1] Goldstein RJ. Film cooling. In Advances in heat transfer. Irvine, TF, Jr, JP Hartnett, editors. Vol. 7, 321–79. New York; Academic press, 1971.
[2] Simoneau RJ, Simon FF. Progress towards understanding and predicting heat transfer in the turbine gas path. Int J Heat and Fluid Flow 1993;14:106–28.
[3] Sinha AK, Bogard DG, Crawford ME. Film-cooling effectiveness downstream of a single row of holes with variable density ratio. J Turbomach 1991;113:442–9.
[4] Sinha AK, Bogard DG, Crawford ME. Gas turbine film cooling: Flowfield due to a second row of holes. J Turbomach 1991;113:450–6.
[5] Pietrzyk JR, Bogard DG, Crawford ME. Effects of density ratio on the hydrodynamics of film cooling. J. Turbomachinery 1990;112:437–43.
[6] Jumper GW, Elrod WC, Rivir RB. Film cooling effectiveness in high-turbulence flow. J Turbomach 1991;113:479–83.
[7] Salcudean M, Gartshore I, Zhang K, McLean I. An experimental study of film cooling effectiveness near the leading edge of a turbine blade. J Turbomach 1994;116:71–9.
[8] Leylek JH, Zerkle RD. Discrete-jet film cooling: a comparison of computational results with experiments. ASME J Turbomach 1994;116:358–68.
[9] Garg VK, Gaugler RE. Effect of coolant temperature and mass flow in film cooling of turbine blades. Int J Heat Mass Trans 1997;40:435–45.
[10] Garg VK, Gaugler RE. Leading edge film cooling effects on turbine blade heat transfer. Num Heat Trans 1996;A30:165–87.
[11] Amer AA, Jubran BA, Hamdan, MA. Comparison of different two-equation turbulence models for prediction of film cooling from two rows of holes. Num Heat Trans 1992;A21:143–62.
[12] Garg VK, Ameri AA. Comparison of two-equation turbulence models for prediction of heat transfer on film-cooled turbine blades. Num Heat Transfer 1997;32A:347–71.
[13] Cruse MW, Yuki UM, Bogard DG. Investigation of various parametric influences on leading edge film cooling. ASME paper 97-GT-296, 1997.
[14] Lin YL, Stephens MA, Shih TI-P. Computation of leading edge film cooling with injection through rows of compound discrete holes. ASME paper 97-GT-298, 1997.
[15] Martin CA, Thole KA. A CFD benchmark study: leading edge film-cooling with compound angle injection. ASME paper 97-GT-297, 1997.
[16] Thakur S, Wright J, Shyy W. Computation of a leading-edge film cooling flow over an experimental geometry, ASME paper 97-GT-381, 1997.
[17] Thakur SS, Wright J, Shyy W, Liu J, Ouyang H, Vu T. Development of pressure-based composite multigrid methods for complex fluid flows. Prog Aerospace Sci 1996;32:313–75.
[18] Shyy W. Computational modeling for fluid flow and interfacial dynamics, Amsterdam, Elsevier: 1994.
[19] Thakur SS, Shyy W, Liou M-S. Convection treatment and pressure splitting for sequential solution procedures. Part

1: theory and one-dimensional test cases. Num Heat Trans 1996;B29:1–27.
[20] Patankar SV. Numerical Heat Transfer and Fluid Flow, Washington D.C., Hemisphere: 1980.
[21] Jones WP and Launder BE. The prediction of laminarization with a two-equation model of turbulence. Int J Heat Mass Trans 1972;15:301–14.
[22] Launder BE, Spalding DB. The numerical computation of turbulent flows. Comp Meth Appl Mech Engg 1974;3:269–89.
[23] Nagano Y, Tagawa M. An improved k–ε model for boundary layer flows. J Fluids Engg 1990;112:33–9.
[24] Youssef MS, Nagano Y, Tagawa MA. Two-equation heat transfer model for predicting turbulent thermal fields under arbitrary wall thermal conditions. Int J Heat Mass Trans 1992;35:3095–104.